Astron. Astrophys. 331, 347–360 (1998)

ASTRONOMY AND ASTROPHYSICS

# The hydrodynamics and ionization structure of gaseous nebulae

## I. The time-dependent solution

**J.A. Rodríguez-Gaspar**[1,2] **and G. Tenorio-Tagle**[3,4]

[1] Instituto de Astrofísica de Canarias, C/ Vía Láctea, E-38200 La Laguna, Tenerife Spain
[2] Astronomisches Institut der Universität Würzburg, Am Hubland, D-97074 Würzburg, Germany (jrg@astro.uni-wuerzburg.de)
[3] Institute of Astronomy, University of Cambridge, Madingley Road, Cambridge CB3 0HA, UK
[4] Royal Greenwich Observatory, Madingley Road, Cambridge CB3 OEZ, UK (gtt@ast.cam.ac.uk)

Received 7 July 1997 / Accepted 27 October 1997

**Abstract.** We present a one-dimensional numerical scheme that allows for the simultaneous solution of the hydrodynamic equations coupled with energy and ionization equations. The code accounts for the time-dependent ionization of H, He, and $He^+$ and for radiative cooling derived from collisional excitation of C, N, O and Ne, whose ionization structures with up to five stages of ionization are calculated under a steady approximation at every time step. Several other physical processes such as collisional ionization, charge-exchange reactions and bremsstrahlung have been taken into consideration. Some assumptions and approximations have been made in order to minimize the computational time. However, the comparison with the results from other steady-state photoionization codes indicates a very precise calculation of the ionization structure. The computational method is meant to be general and allows for a wide variety of ionizing sources (e.g. a black body, a stellar atmosphere model and a power law) as well as their possible evolution in time. The code is supplemented with the necessary tools to calculate the synthesized spectrum from the numerical models, including the most important lines of the elements mentioned in order to compare directly with the observations. In this paper the code is described and the first calculations for the standard evolution of H II regions are shown. The results generally agree with previous works but in addition they go to greater depth showing some interesting aspects of the evolution of gaseous nebulae.

**Key words:** H II regions – ISM: kinematics and dynamics – radiative transfer – atomic processes

### 1. Introduction

The theory of the evolution of H II regions has been developed with a variety of analytical and numerical studies (see review by Yorke 1986, and the standard reference books by Osterbrock 1989 and Spitzer 1978). Although a considerable degree of physical complexity has been attained in steady-state solutions of the ionization structure (Harrington et al. 1982; Ferland 1990), most hydrodynamic models have been quite approximate in their treatment of the radiative transfer and the solution of the energy and ionization equations (Mathews 1965; Tenorio-Tagle 1976; Manfroid 1976; Bodenheimer, Tenorio-Tagle & Yorke 1979). However, these numerical models together with the analytical studies based on autosimilar solutions, have composed a complete picture of the dynamical evolution of H II regions in the "standard case", i.e. under the assumption of a constant-density medium and a constant ionizing photon flux. Thus, when a massive ionizing star enters the main sequence, its UV photons create a supersonic weak-R type ionization front (IF, see Spitzer 1978 for a classification of IFs) that moves through the gas, leaving it hot and ionized but dynamically unperturbed. When the ionized region has reached its Strömgren radius ($R_{\rm s}$), the dimension of the volume within which the number of recombinations equals the UV stellar photon output (Strömgren 1939), the large pressure gradient across the IF causes the expansion of the H II region. The expansion is supersonic with respect to the ambient neutral material and creates a shock wave that accelerates and piles up the neutral gas into a dense shell.

Departures from the classical evolution during the phases of formation and expansion, as outlined above, have been studied by changing the initial distribution of density or by simulating the UV flux turn-off when the star leaves the main sequence. Studies of evolved H II regions after the star flux begins to decline (Beltrametti, Tenorio-Tagle & Yorke 1982, hereafter BTY, and Tenorio-Tagle et al. 1982, hereafter TBBY) have shown how the decrease in the ionizing flux causes the IF to recede supersonically towards the star. Once the recession speed of the IF becomes comparable to $c_i$ the ionized gas can react to the pressure gradient across the IF and a second expansion of the ionized region begins. This picture undergoes a further variation with the inhibition of the reionization phase for low values of the

*Send offprint requests to*: J.A. Rodríguez-Gaspar

initial density (see TTBY). The relaxation of the assumption of constant ambient density leads to the well-known "champagne" phase when an IF overruns a density gradient and the large pressure gradient found within the ionized gas leads to the disruption of the densest medium (Tenorio-Tagle 1979). Numerical and analytical studies of this phase have shown that it can produce highly supersonic flows. Franco, Tenorio-Tagle & Bodenheimer (1990) also showed that for a cloud with a power-law density distribution ($\rho \propto r^{-w}$) the evolution can follow the classical scheme of IF + shock ($w < 3$) or the champagne phase ($w > 3$). In a more recent paper Rodríguez-Gaspar, Tenorio-Tagle & Franco (1995) calculated the optical appearance of these regions in $\lambda$ 5007 and H$\alpha$ showing that during the champagne phase the formation of these lines may arise from different sectors of the flow. Yorke, Tenorio-Tagle & Bodenheimer (1983, 1984) also calculated the optical and radio maps of 2-D models of the champagne phase (Bodenheimer et al. 1979 and Tenorio-Tagle 1979). All these line-transfer calculations based on the numerical output of hydrocodes that considered only the ionization of hydrogen clearly had to make strong assumptions on the ionization structure of H II regions.

Here we present an efficient method for solving the equations of hydrodynamics coupled with a detailed description of the temperature and ionization structure of a nebula. The method is meant to be general enough to allow for any source of ionization as well as possible intrinsic time variations in their spectra. Moreover, the necessary tools to calculate quantities directly comparable with the observations have been installed.

In Sect. 2 we present the general equations and approximations made to handle both the hydrodynamic and line-transfer equations. Sect. 3 presents the tests performed on the code and a comparison with the results from CLOUDY; a widely used steady-state photoionization code. Sect. 4 is a review of the classical evolution of an H II region in a low constant density medium focusing on the calculated observables (such as surface brightness, line profiles, as well as their spatial distribution, and diagnostic diagrams). Finally, Sect. 5 summarizes our main conclusions and future work. The treatment of the diffuse field and the calculation of the line transfer are given as appendices.

## 2. Numerical scheme

The hydrodynamical equations coupled with the energy and ionization equations are solved with a finite-difference method, originally described by Tenorio-Tagle, Bodenheimer & Noriega-Crespo (1986). The method is an extension of a previous one (Tenorio-Tagle 1976) that accounted only for the ionization of hydrogen, and the radiative transport was realized through the "grey" approximation at the hydrogen threshold frequency ($h\nu_0$ = 13.6 eV). The new method accounts for the time-dependent ionization of hydrogen and helium and radiative cooling by collisionally excited lines, obtained from the ionization structure of carbon, nitrogen, oxygen and neon, calculated under a steady-state approximation, at every time step. Other processes such as bremsstrahlung, collisional ionization and a chain of charge-exchange reactions have been considered. The ionizing radiation field can have different spectral forms (from a black body to a power-law, etc.), and the method allows for its evolution as a function of time. For the diffuse radiation field, able to ionize both hydrogen and helium, one of two different approximations has been made: either the on-the-spot approximation (OTS) was assumed for both hydrogen and helium, or the diffuse field was transported under the assumption of the outward only approximation (see Williams 1967). The description of both approximations is given in appendix A, and a comparison of the results obtained using both possibilities is given in the Sect. 3.

The hydrodynamic equations are written in a finite-difference Lagrangian formulation (see Tenorio-Tagle et al. 1986) following the scheme described by Richtmyer & Morton (1967). A non-linear artificial viscosity term has been used in order to smooth shocks over several grid points.

The ionization equations of $H^0$, $He^0$ and $He^+$ are solved simultaneously with the energy equation by a Newton-Raphson iteration. The equation of state and the energy equation are,

$$p = \frac{k\,T\,\rho\,\Theta}{\mu m_{\rm H}}, \tag{1}$$

$$\frac{dT}{dt} = -\frac{T}{\Theta}\frac{d\Theta}{dt} - (\gamma-1)\left\{T\rho + \frac{\mu m_{\rm H}\,Q}{k\,\Theta}\right\}\frac{d(1/\rho)}{dt} + (\gamma-1)\frac{\mu m_{\rm H}}{k\,\Theta\,\rho}\left\{\sum_h \Gamma^h - \sum_c \Lambda^c\right\}. \tag{2}$$

Here temperature ($T$) was adopted as the hydrodynamic variable instead of the frequently used internal energy ($\varepsilon = 1/(\gamma - 1) \times k\,T\,\rho\,\Theta/\mu m_{\rm H}$). The factor $\gamma$, which accounts for the gas-particle degrees of freedom was set to $^5/_3$, corresponding to a monoatomic gas. The summations in Eq. (2) on $h$ and $c$ indicate different heating and cooling mechanisms.

The ionization equations of $H^0$, $He^0$ and $He^+$ take into account radiative recombination and all processes that can cause ionization and lead to the time-dependent equations

$$\frac{dx}{dt} = (1-x)\left\{\sum_{f=s,d}\Upsilon^f_{\rm H^0} + n_e\,C_{\rm H^0}\right\} - x\,n_e\,\alpha_{B,\rm H^0}$$

($H^0$ ionization), (3)

$$\frac{dy}{dt} = w\left\{\sum_{f=s,d}\Upsilon^f_{\rm He^0} + n_e\,C_{\rm He^0}\right\} + z\,n_e\,\alpha_{A,\rm He^+} - y\left\{n_e\alpha_{A,\rm He^0} + n_e\,C_{\rm He^+} + \sum_{f=s,d}\Upsilon^f_{\rm He^+}\right\}$$

($He^0$ ionization), (4)

$$\frac{dz}{dt} = y\left\{\sum_{f=s,d}\Upsilon^f_{\rm He^+} + n_e\,C_{\rm He^+}\right\} - z\,n_e\,\alpha_{A,\rm He^+}$$

($He^+$ ionization). (5)

The summation on $f$ indicates the contribution from the stellar radiation field ($s$) and the diffuse radiation field ($d$). To

resume, and to offer a better explanation of the whole set of variables, we list below the symbols used and give a brief explanation of their meanings:

$k$ = Boltzmann constant,
$p$ = pressure,
$\rho = n\mu m_{\rm H}$ and $n = n_{\rm H} + n_{\rm He}$ = total mass and particle number density, respectively,
$\mu m_{\rm H} = f_{\rm H} m_{\rm H} + f_{\rm He} m_{\rm He}$ = mean molecular weight,
$m_m$ = atomic masses of the various elements in grams,
$f_m = n_m/n$ = relative abundances,
$n_e = n\,[f_{\rm H} x + f_{\rm He}(y + 2z)]$ = density of free electrons,
$T$ = temperature,
$Q$ = artificial viscosity,
$\Theta = (f_{\rm H} + f_{\rm He}) + n_e/n$ (term that accounts for the total number of particles: atoms, ions and electrons),
$x, w, y, z$ = ionization degree of $H^0$, $He^0$, $He^+$ and $He^{2+}$ respectively, with $w + y + z = 1$,
$\Upsilon$ = photoionization rates,
$C$ = collisional ionization rates,
$\alpha$ = recombination rates,
$\Gamma$ = heating rates, and
$\Lambda$ = cooling rates.

### 2.1. Ionizing flux

The ionizing source is located at the centre of the computational grid ($R = 0$) and we assume that its dimensions are negligible compared with other scales involved in the problem. The photoionization rate of an $i$ ion to an $i + 1$ ion can been written as

$$\Upsilon_i = \int_{\nu_i}^{\infty} \frac{4\pi J_\nu}{h\nu}\, a_{\nu,i}\, d\nu, \tag{6}$$

and the corresponding heating rates in the Eq. (2) are

$$\Gamma_i^{\rm phot} = \int_{\nu_i}^{\infty} \frac{4\pi J_\nu}{h\nu} h(\nu - \nu_i)\, a_{\nu,i}\, d\nu, \tag{7}$$

where $\nu_i$ is the ionization threshold frequency, $a_{\nu,i}$ is the photoionization cross-section from the ground level and $J_\nu$ is the mean intensity of the radiation. This radiative field is composed of two parts: $J_\nu = J_\nu^s + J_\nu^d$, the field $J_\nu^s$, produced by the central source and the diffuse field $J_\nu^d$, produced through recombinations. If we assume that the central source is a star with radius $R_\star$ and an emergent flux $\pi F_\nu^\star(R_\star)$, the radiative transport equation is

$$4\pi J_\nu^s = \pi F_\nu^s(R) = \left(\frac{R_\star}{R}\right)^2 \pi F_\nu^s(R_\star) e^{-\tau_\nu}. \tag{8}$$

The optical depth $\tau_\nu = \sum_{i={\rm H^0,He^0,He^+}} n_i a_{\nu,i}$ is measured from the central source position and is dominated by the most abundant elements in the region, hydrogen and helium. The contribution from heavier elements is negligible due to their low abundance. All photoionization terms $\Upsilon_i^s$ and the corresponding heating terms $\Gamma_i^{{\rm phot},s}$, i.e. all the integral terms in the ionization and energy equations, can be determined as a function of one single parameter if the photoionization cross-sections of the $H^0$, $He^0$ and $He^+$ have the same frequency dependence. The assumption made here for three frequency intervals is shown in Fig. 1. In this way all the integral terms of photoionization can be calculated prior to their use in the time-dependent calculations and stored, ready to use, in tables as functions of a single parameter; the optical depth. This approximation saves an enormous amount of computational time.

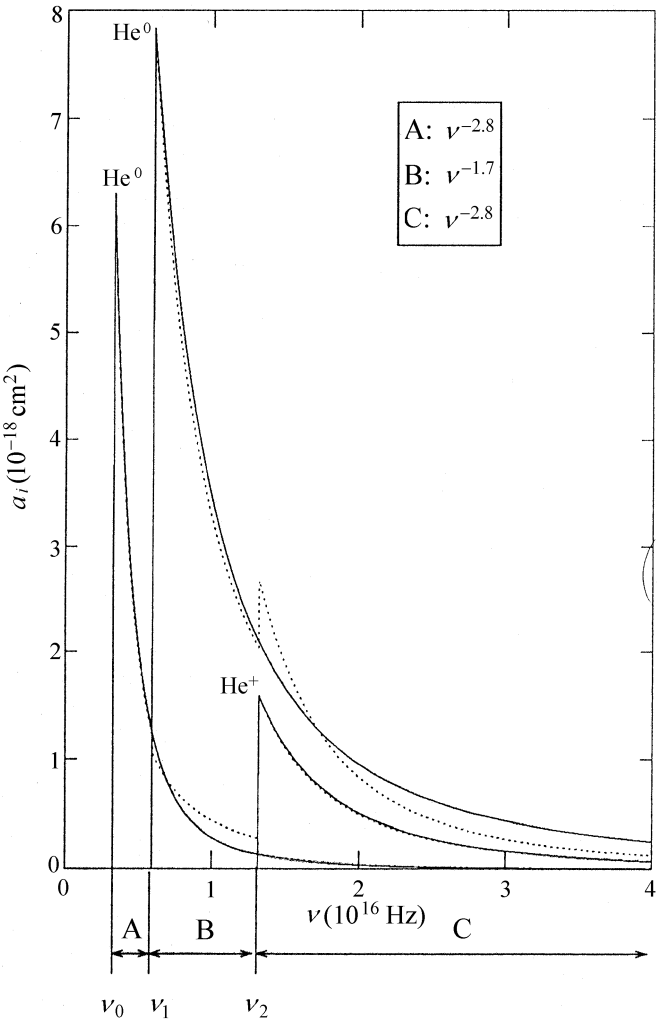


**Fig. 1.** The solid lines are the photoionization coefficients for $H^0$, $He^0$ and $He^+$ according to the empiric formula of Seaton (1958). The dotted line are the approximations used in each of the three selected frequency intervals. In the box the adopted frequency dependence for each interval is given.

### 2.2. Physical processes

Several microphysical processes are considered in the numerical scheme. Here we discuss the different approximations, our choice of numerical coefficients and their range of validity. As a general rule we have looked for simple analytic formulae to obtain the fastest computational speed.

*Recombination.* We have used the expressions given by Seaton (1959) in the hydrogenic approximation to the radiative recombination coefficients $\alpha$ and those averaged in energy $\beta$ for $H^+$, $He^+$ and $He^{2+}$. For the recombination coefficients of heavier elements, $\alpha_m^{+k}$ (where $m$ indicates the element and $k$ indicates the ion), from the ground level of the ion ($m$,$k+1$) to all levels of the ion ($m$,$k$), a good empirical fit is given by Aldrovandi & Pequinot (1973), which includes both the radiative and the dielectronic contribution.

*Collisional ionization.* For the collisional ionization coefficients $C(m,k)$ the expression given by Canto & Daltabuit (1974) have been used taking the numerical values of Franco (1981).

*Charge-exchange reactions.* For the charge-exchange reactions of heavy elements with hydrogen and helium we have used the rate coefficients tabulated as a function of temperature by Butler, Heil & Dalgarno (1980) and Butler & Dalgarno (1980).

*Cooling by collisionally excited lines.* The most important cooling source in H II regions is emission through the collisionally excited lines of heavy elements. In order to obtain this cooling, the ionization structure of carbon, nitrogen, oxygen and neon is calculated. It requires that in each position in the nebula the ionization number be equal to the recombination number to all levels. For two successive ionization states, $k$ and $k+1$, of every element we can calculate the relation

$$\frac{n_{m,k+1}}{n_{m,k}} = \frac{\Upsilon^{\rm phot}_{m,k} + n_e C_{m,k}(T) + \sum_{i,j} n_{i,j}\delta(m,k,i,j)}{n_e \alpha_{m,k}(T) + \sum_{i,j} n_{i,j}\delta(m,k+1,i,j)}, \qquad (9)$$

where $\Upsilon_{m,k}$ is the photoionization rate from the ground level of the ion ($m$,$k$) with a threshold frequency $\nu_{m,k}$. For the photoionization cross-sections $a_{\nu,m,k}$, we have used a linear interpolation of the tables given by Reilman & Manson (1979). The set of equations (9) for each element together with

$$\sum_k n_{m,k} = n_m = f_m n, \qquad (10)$$

where $f_m$ is equal to the selected abundance, here assumed constant across the nebula, allows the determination of the ionization structure of the element. Once the ionization structure has been calculated, the cooling through forbidden-line radiation is obtained by solving the two-level approximation for the population levels of each ion. Thus for level $i$ we have

$$\Lambda^{\rm line} = n_e \sum_{m,k,l} \frac{n_{m,k} q_{m,k,l} h\nu_{m,k,l}}{1 + n_e q'_{m,k,l}/A_{m,k,l}}, \qquad (11)$$

where $q_{m,k,l}$ are the collisional excitation and de-excitation rates and $A_{m,k,l}$ are the radiative decay rates respectively for the transition $l$ between the levels $n = 1$ and $n = 2$. The values tabulated by Mendoza (1983) for $q_{m,k,l}$ and $A_{m,k,l}$ were used.

Moreover *bremsstrahlung*, or *free-free emission* produced by the deceleration of electrons in the Coulomb field from the atoms of hydrogen and helium has been included.

*Cooling in the neutral gas.* When the fractional ionization due to photoionization is low ($x \lesssim 10^{-4}$), other cooling sources operate in the neutral gas: excitation by impact of hydrogen neutral atoms on the fine-structure lines of $C^+$, $O^0$, $Si^+$ and $Fe^+$. As the code does not account for the ionization of some of these elements, the interstellar cooling law from Dalgarno & Mc Cray (1972) has been used in this range of ionization degree.

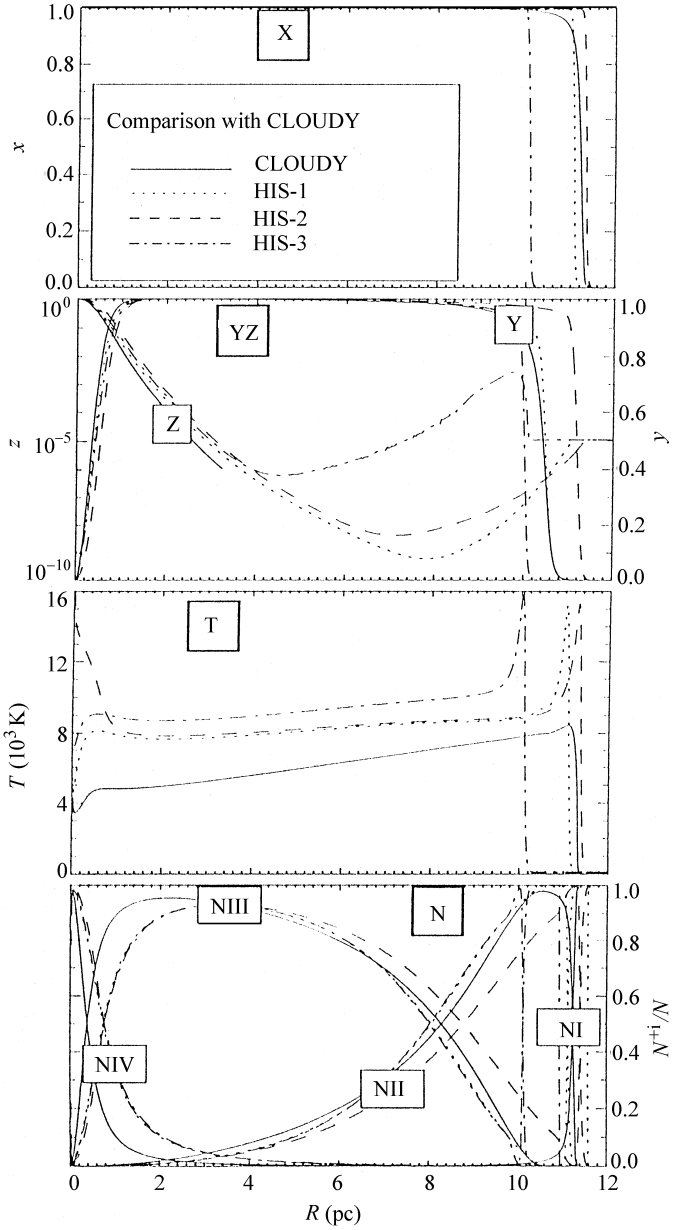


**Fig. 2.** Comparison with CLOUDY. From top to bottom the panels show: (X) degree of ionization of $H^+$, (YZ) degrees of ionization of $He^+$ and $He^{2+}$, (T) the temperature distribution and (N) the ionization structure of nitrogen.

## 3. Test calculations

Many tests have been performed in order to check the reliability of the code. The hydrodynamic scheme, coupled with simple ionization structures, had already been implemented to solve many astrophysical problems (see Sect. 2). However, the calculation of the ionization structure with several elements, several ionization stages and a frequency dependent radiative transport, require further checks in order to warrant its accuracy. The most feasible comparison is with widely used steady-state photoionization codes, such as CLOUDY (Ferland 1990). CLOUDY includes a large number of physical processes and has a high accuracy on photoionization calculations. To compare both codes, the same initial conditions were used, i.e. a constant-density medium with $\rho = 10\mu m_{\rm H}$, a star with a blackbody spectrum of 40000 K and a radius of $5 \times 10^{11}$ cm. The selected heavy element abundances with respect to hydrogen, were those CLOUDY uses by default for H II region calculations: helium, 0.0095; carbon, $3.71 \times 10^{-4}$; nitrogen, $1.176 \times 10^{-4}$; oxygen, $6.76 \times 10^{-4}$; and neon, $1.082 \times 10^{-4}$.

Fig. 2 shows the comparison with CLOUDY. The various curves correspond to the ionization degree of hydrogen (labelled X), helium (labelled Y and Z; to indicate the distributions of $He^+$ and $He^{2+}$, respectively), temperature (T) and the ionization structure of nitrogen (N). Three different models (identified with the acronym HIS, which stands for *h*ydrodynamics and *i*onization *s*tructure, and a number) were calculated in order to compare with CLOUDY. The different models show results obtained with different approximations to the treatment of the diffuse radiation field (see Appendix A for a detailed description of the approximations). HIS-1 applied the OTS approximation only to hydrogen, in HIS-2 the OTS approximation was used for both hydrogen and helium, and in HIS-3 the diffuse radiation was treated in the outward approximation. All our models were calculated time dependently from $t$ = 0, until the leading IF reached the Strömgren radius and a shock began to develop (t $\sim 2 \times 10^4$ yr). Note that there are slight differences in the position of the IF between the various models. This is due to the slightly different times at which the calculations were stopped. Note also that for HIS-3, the hydrogen (X) IF is located $\sim$ 1 pc behind the other IFs. This is due to the greater pressure at the IF, caused by the larger temperature established through photoionization, which leads to an earlier development of the outer shock in this case. At $2 \times 10^4$ yr the IF reached in HIS-3 the Strömgren radius ( $\sim$ 11 pc) but its structure was modified by the emergent shock, and hence the different conditions inhibit a clear comparison with CLOUDY.

The $H^+$ and $He^+$ ionization fronts (X and Y in Fig. 2) in our models present a steeper profile than in CLOUDY. This is due to the fact that recombinations there have not had enough time to balance the ionization, and the IF width is close to its theoretical value ($\sim (na_\nu)^{-1} \approx 10^{16}$ cm); the photon mean free path. However, the IFs of $He^{2+}$ soon reaches equilibrium and resembles the output from CLOUDY (Z in Fig. 2).

There are slight differences between $\sim$ 4 pc and $R_{\rm s} \approx$ 11 pc, at low-level values of $z$ (shown on a logarithmic scale), between the different runs. Note that a full comparison with CLOUDY in this zone was not possible as CLOUDY sets $z$ to 0 whenever its value falls below $\sim 10^{-6}$. The increase in $He^{2+}$ for HIS-2 is due to ionization of $He^+$ through the high-energy tail photons produced by recombinations to the ground level of $H^0$ and $He^0$. The enhancement increase in HIS-3, of nearly three orders of magnitude, results from photons produced by recombinations to the ground level of $He^+$, occurring at the inner $He^{2+}$ zone and whose ionizing photons under the OTS approximation (HIS-2) are absorbed locally. By way of contrast, in the outward approximation (HIS-3) these photons penetrate deeper into the region to be absorbed in the outer parts, increasing the value of $z$ up to $10^{-3}$ at the IF (see curve Z in Fig. 2 and to note that the $z$-scale is logarithmic).

The temperature distributions of the HIS and CLOUDY models (Fig. 2) show a gradual increase towards the edge due to the hardening of the radiation. However, the most conspicuous difference is the existence of a temperature peak at the IF with a temperature of $\gtrsim$ 15000 K in our models which does not appear in CLOUDY. This is an important characteristic of the time-dependent calculations and is caused by the cooling length that newly ionized gas needs to approach the equilibrium temperature of the H II region. There is, however, a substantial discrepancy between CLOUDY and HIS of almost 3000 K in the inner regions dropping to 1000 K at the IF. These differences, we believe arise from the inclusion in CLOUDY of further cooling agents, such as Lyman $\alpha$, and perhaps by the more accurate treatment than our two-level atom approximation for the collisionally excited lines. Both will be the subject of further improvements in our code.

The various approximations to the treatment of the diffuse radiation field also led to some temperature differences between our models (see Fig. 2). In HIS-1 the temperature falls at the centre down to 4000 K due to the cooling through the $25\mu m$ line of the $O^{3+}$. However, for HIS-2 the temperature at the centre rises to 15000 K. This increment is caused by the photons produced by the recombinations to excited levels of $He^+$ ($h\nu$ = 40.8 eV) which are entirely absorbed in this zone. In HIS-1 these photons were not taken into account. Rubin (1968) showed that the effect of the OTS approximation on the central part of the region was exactly the opposite. The OTS approximation overestimated the radiation field in the central part and the fraction of neutrals was lowered and hence the photoheating. As a consequence the temperature falls to 2000 K at the centre. Rubin, however, did not account for the ionization of $He^+$ to $He^{2+}$, nor its recombinations, which are what cause the heating. The outward approximation in HIS-3 avoids this problem by allowing the transport of these photons farther into the nebula. Thus the central peak vanishes and the equilibrium temperature is increased in the whole region through heating by diffuse photons. Finally, Fig. 2 also compares the ionization structure of nitrogen. Note that except for slight differences at the N IV–N III interface the structure for HIS-1, HIS-3 and CLOUDY are identical. HIS-2 presents slight deviations at the N III–N II interface because the optical depth is lowered by the $He^0$ depletion produced by the diffuse photons.

This lower optical depth allows a slightly larger zone of N III and $He^+$ (Y in Fig. 2).

The comparison of our time dependent models with CLOUDY is more than satisfactory. All the variables calculated with HIS-1 coincide well with the output from CLOUDY. Inclusion of the diffuse radiation due to helium leads to slight discrepancies which will require further analysis. CLOUDY gives a very different treatment of the diffuse radiation through local escape probabilities but without considering further ionizations. This could explain the similarity between CLOUDY and our HIS-1 model where the diffuse radiation arises only through hydrogen recombination.

## 4. Results

### *4.1. Hydrodynamic evolution*

Given the agreement between CLOUDY and our time-dependent approach, we have calculated the evolution of an H II region long past the main-sequence lifetime of its ionizing source, using the same initial conditions as indicated in the previous section.

At $t = 0$ the ionizing flux is suddenly turned on and the IFs of hydrogen and singly ionized helium supersonically outrun the neutral gas. During this stage the hydrogen IF is of weak-R type, so the ionized and the neutral gas see it advancing at supersonic velocity. Fig. 3a shows the position of the IFs during the early formation phase, across the still unperturbed density distribution of the region. At $t \sim 1/(n\alpha_B(\mathrm{H}^0)) \sim 2\times10^4$ yr, the recombination timescale, the IF has almost reached the Strömgren radius and its velocity is about $\sim 2c_i$ (twice the sound speed in the ionized gas) due to the diminishing number of photons suffered both by geometrical dilution (the radiation flux is $\propto R^{-2}$) and recombination. The gas then begins to feel the pressure gradient across the IF, and as a consequence a shock ($S_1$ in Fig. 3b) develops and the expansion phase begins. After this, the IFs of $H^+$ and $He^+$ cease to coincide with one another. The expansion phase (panels B) is characterized by a weak-D IF+shock configuration where the IF moves subsonically with respect to both the ionized and the shocked neutral gas. The expansion induces a rarefaction wave into the ionized volume which effectively begins to lower the density ($RW_1$ in Fig. 3b). At time $t = 10^6$ yr, we have assumed that the stellar flux begins to decrease as $t^{-m}$ with $m = -5$. This is meant to represent approximately the decreasing flux from an O star during its post-main sequence evolution (see BTY). The decrease in the flux forces the IFs to recede supersonically towards the stars (see Fig. 3-C), causing the recombination of a large volume of expanding gas. The IF width (Fig. 3d) is now given by the distance that an ion can travel before it recombines $\sim u/(n\alpha_B(\mathrm{H}^0))$. The gas speed flowing through the IF is about $10 - 18$ km s$^{-1}$, $n$ is about $\sim 1$ cm$^{-3}$ caused by rarefaction and $\alpha_B(\mathrm{H}^0) \sim 3\times10^{-13}$ cm$^{-3}$ s$^{-1}$, which gives a width of $> 1$ pc. This extended IF produces an extended or more continuous pressure gradient which re-accelerates the newly recombined gas outwards, the development of a strong rarefaction wave ($RW_2$ in Fig. 3d) driven by the receding IF then originating.

When the outermost shell of shocked neutral gas stops feeling the pressure of the ionized gas, an 'N' wave forms (see BTY). The pressure in the neutral shell is larger than in its immediate surroundings both ahead and behind it, and this causes a new shock, $S_2$, moving inwards towards the star, and a rarefaction wave ($RW_3$) which lowers the density of the leading shell. The shock $S_2$ decelerates the newly recombined gas, previously accelerated by the receding IF and piles it up in an increasingly broader zone just behind the leading shell. Note that the zone between $S_1$ and $S_2$ is composed of two layers of different densities ($n(S_1) \sim 10^3$ cm$^{-3}$ and $n(S_2) \sim 1$ cm$^{-3}$). Inside the H II region the rarefaction waves $RW_1$ and $RW_2$ have lowered the density even further ($n \sim 1$ cm$^{-3}$) and as a consequence the recombination rate is slower. This, together with the larger photon flux found nearer the star slows down the receding IFs. This happens up to a point when their recession velocity, with respect to the gas, $V_{\rm IF} - u$, is less than $c_i$ and the pressure gradient across the IF then has enough time to cause an outward acceleration. The pressure profile then steepens and a new shock ($S_3$) develops. At the same time the shock formation generates a new rarefaction wave ($RW_4$) moving inwards. This lowers the density and inhibits further the recombination. Consequently, a new supply of photons (despite the continuous decrease in the stellar photon flux) can reach the IF. In this way the IF stops its recession and turn back to reionize the recombined gas while driving the new shock, $S_3$, outwards. The system IF + shock during this reionization stage is similar to that of the first expansion phase, except that the shock now travels into an expanding medium. The IF + shock system travels more quickly than the outer shocks because the density of the H II regions decreases faster than the stellar flux as a consequence of successive rarefactions. Eventually the shock $S_3$ interacts with the reverse shock $S_2$ producing a shock reflexion. Two new shocks $S_2'$ and $S_3'$ then form and pile up the low-density ionized gas against the layer of shocked neutral gas behind $S_1$. The calculations were stopped at the point when the IF started pushed the shock $S_1$ again. The further evolution is characterized by an extremely low-density H II region which finally recombines because of the assumed continuous drop in the ionizing flux.

During the late evolutionary stages, the radius of the external shock does not evolve following the classical formula

$$R_{\rm IF}(t) = R_{\rm s}\left(1 + \frac{7}{4}\frac{c_i(t - t_{\rm form})}{R_{\rm s}}\right)^{4/7}, \qquad (12)$$

because by then it is not the pressure of the ionized gas that drives it but rather its own inertia. Even when the IF and the new shock, $S_3$, catch up with the external layer, the density of the H II region is so low that the pressure of the ionized gas just equals the external pressure. Thus one can assume that all the gas of the nebula is contained in a thin layer and since the momentum conservation

$$\frac{d(4/3\pi R_{\rm sh}^3\rho_{\rm sh})}{dt} = 0, \qquad (13)$$

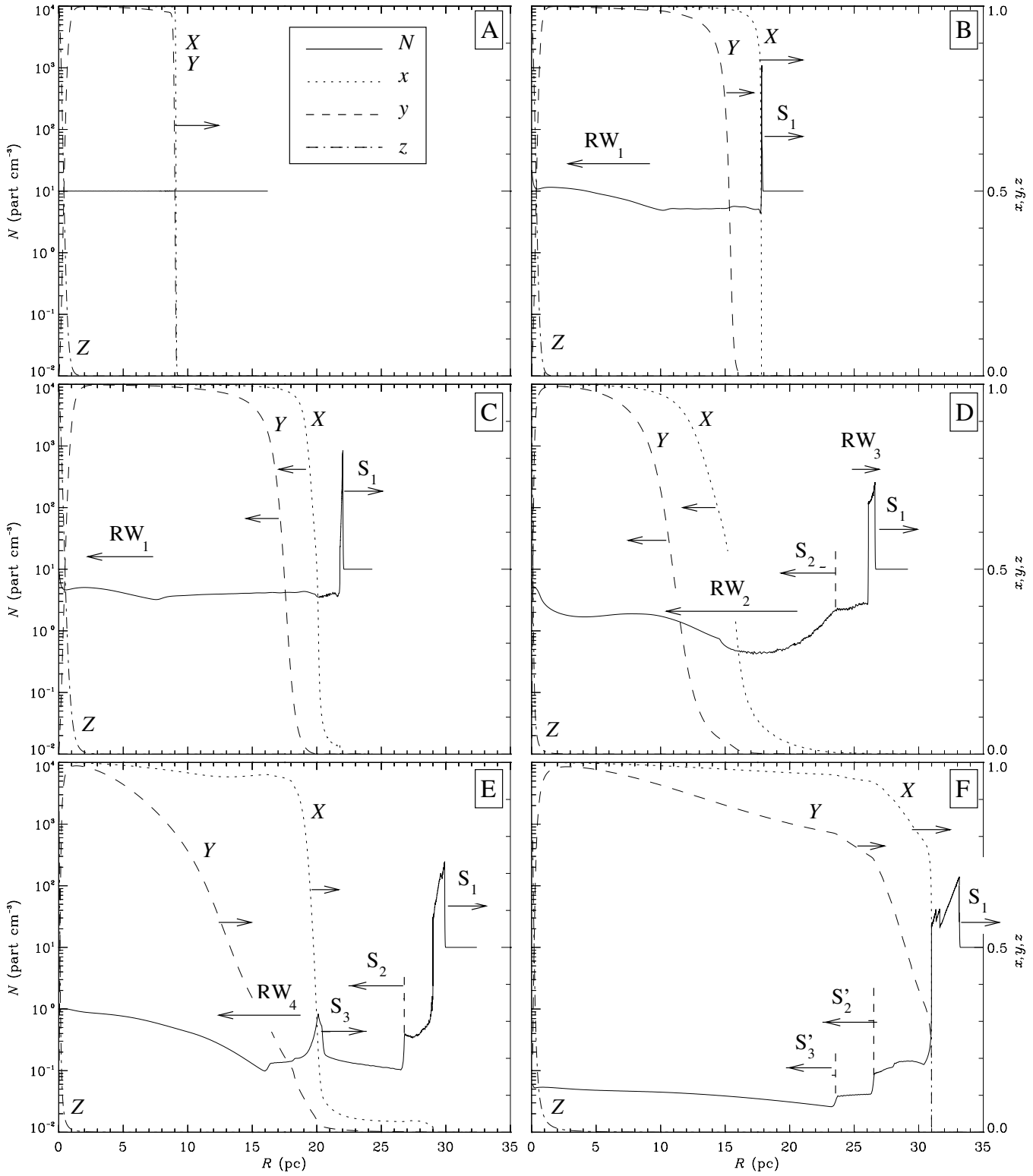


**Fig. 3a–f.** The evolution of H II regions. Density (solid line) and the ionization structure of hydrogen (dashed line; labelled X), and singly (dashed line labelled Y) and doubly ionized helium (dash-dotted line; labelled Z) at various evolutionary ages: **a** $8.0 \times 10^3$, **b** $6.0 \times 10^5$, **c** $1.0 \times 10^6$, **d** $2.0 \times 10^6$, **e** $2.8 \times 10^6$ and **f** $3.5 \times 10^6$ yr. The various shocks (S) and rarefaction waves (RW) that appear in the flow, as well as their direction of motion are indicated in the plots

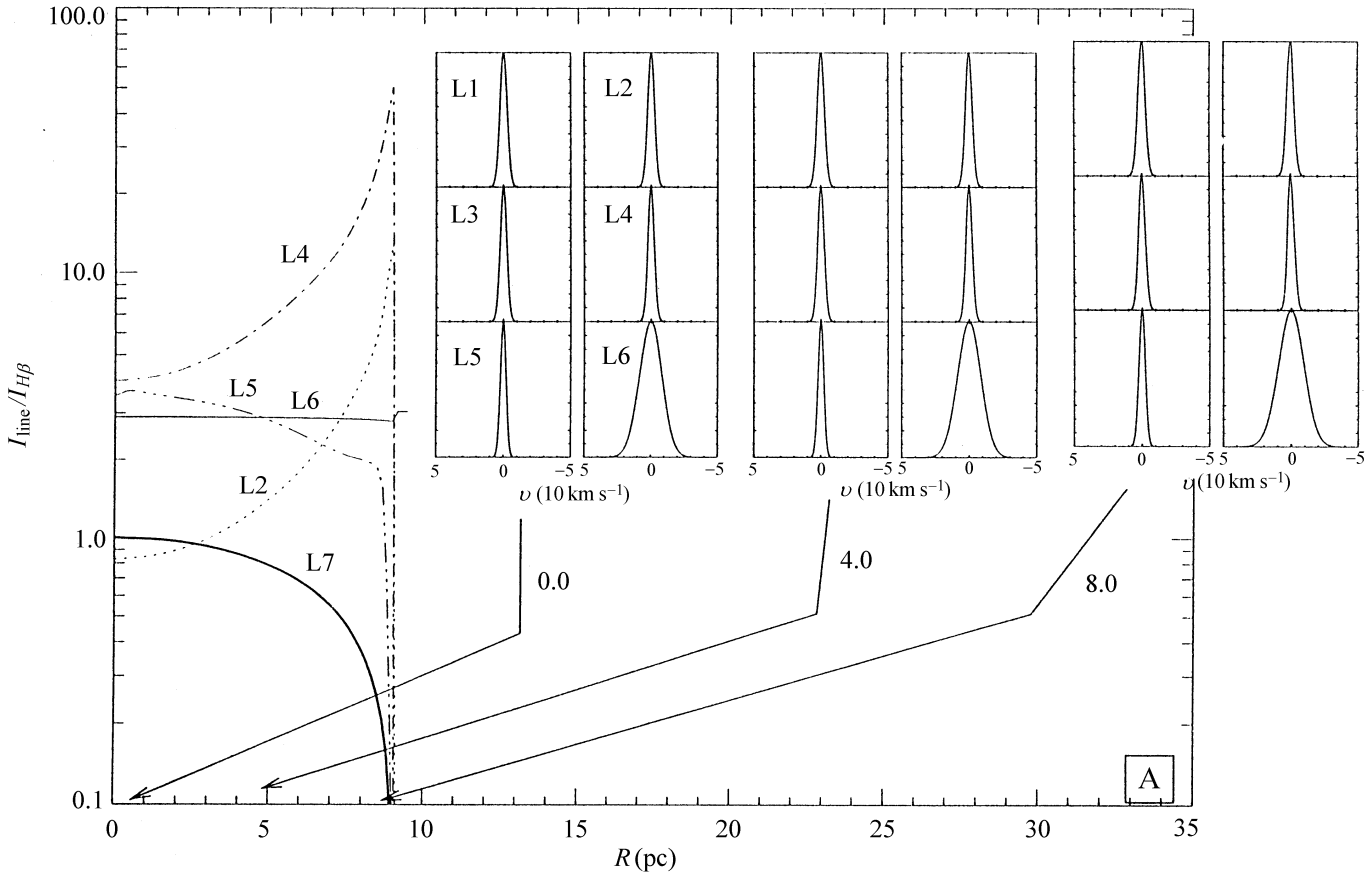


**Fig. 4.** Surface brightness relative to H$\beta$ and line profiles (inner squares) for model A (see Fig. 3). The line codification is as follows: (L1) [N I] $\lambda$ 5200, (L2) [N II] $\lambda$ 6584, (L3) [O I] $\lambda$ 6300, (L4) [O II] $\lambda$ 3727, (L5) [O III] $\lambda$ 5007, (L6) H$\alpha$ and (L7) H$\beta$. The line profiles are integrated at different impact parameters across the nebula indicated by the arrows on the $x$-axis. The numerical values of the impact parameters is indicated in pc on the arrows. The line profiles of H$\beta$ have not been included in the plot since they are nearly identical to those of H$\alpha$. The thick black line is the surface brightness of H$\beta$ normalized to its maximum value at that evolutionary time.

which implies

$$R_{\rm sh} = R(t_{\rm turn}) \left[1 + \frac{4U(t_{\rm turn})(t - t_{\rm turn})}{R(t_{\rm turn})}\right]^{1/4}, \qquad (14)$$

where $t_{\rm turn}$(= $10^6$ yr) is the time when the star leaves the main sequence. When the velocity of this layer drops below the sound velocity in the neutral medium, $c_n$, the shock $S_1$ will decay into a sound wave and the dynamical effect of the original H II region will have finished. Setting $\dot{R}_{\rm sh}(t_{\rm end}) = c_n$ we can obtain the time $t_{\rm end}$ when the evolution ends:

$$t_{\rm end} = t_{\rm turn} + \frac{R(t_{\rm turn})}{4U(t_{\rm turn})} \left[\left(\frac{U(t_{\rm turn})}{c_0}\right)^{4/3} - 1\right]. \qquad (15)$$

Substituting values, it is found that $t_{\rm end} = 1.7 \times 10^7$ yr for a final radius of $R_{\rm sh}(t_{\rm end}) = 4.3 R_{\rm s}$.

Our calculations confirm the earlier results from BTY and TBBY. In particular, during the formation and expansion phases our results matches the well-known theory of the evolution of H II regions exactly. We have also calculated the short recombination and reionization phases, generated during the massive star excursion away from the main sequence. During recombination we find very extended IFs (or rather recombination fronts) with a width $\sim u/(n\alpha_B(\mathrm{H}^0))$ (i.e. dependent on the gas velocity), which drive further rarefaction waves into the ionized volume. Our method thus recovers all dynamical events in the evolution of H II regions and furthermore, given the more complete approach to the problem, offers many more possibilities for direct comparison with the observations.

### *4.2. Optical appearance of evolving H II regions*

To compare with the observations we have selected two basic observational magnitudes, the surface brightness with respect to H$\beta$, i.e. the luminosity in a given line as a function of radius, which supplies information about the physical conditions in the nebula (density, ionization, temperature, etc), and line profiles, which are related to the kinematic state of the nebula. It is important to notice that this is only possible from the numerical output of a hydrocode that calculates both the hydrodynamics and the ionization structure of the nebula (see appendix B for details on the line transfer calculations). The surface brightnesses are referred to H$\beta$; the usual presentation of observational re-

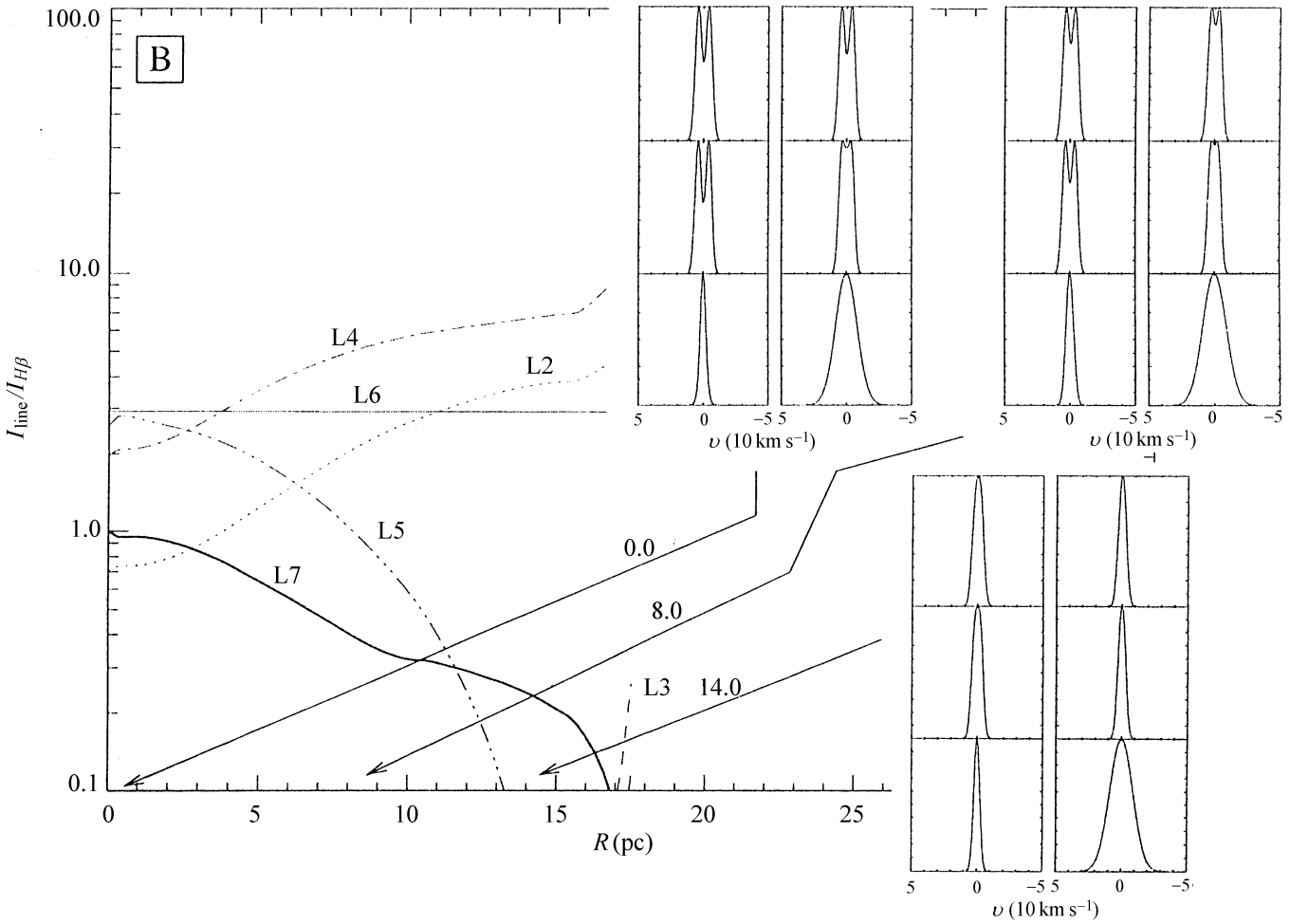


**Fig. 5.** Surface brightness relative to H$\beta$ and line profiles for the model B (see Fig. 3). The symbols and arrows have the same meaning as in the Fig. 4.

sults. The lines selected were: (L1) [N I] $\lambda$ 5200, (L2) [N II] $\lambda$ 6584, (L3) [O I] $\lambda$ 6300, (L4) [O II] $\lambda$ 3727, (L5) [O III] $\lambda$ 5007, (L6) H$\alpha$ and (L7) H$\beta$. Several other lines from C, N, O and Ne were calculated but those listed above are among the most frequently used in observational studies of H II regions. Although our models are one-dimensional, they can supply important trends or traces of the possible stage of evolution of an H II region. Most of the observational information about H II regions is in form of integrated or global quantities (except in cases with excellent spatial resolution), hence deviations from spherical symmetry and those caused by inhomogeneities may not be so important. We regard our results as an excellent standard reference frame for future observational and theoretical work.

Fig. 4 shows the results for the H II region during its formation phase. The surface brightness of $\lambda$ 5007 present a core distribution with the maximum at the centre and a smooth declination towards the edge. However, $\lambda$ 6584 and $\lambda$ 3727 present radial distributions with a central depression and a sharp rise towards the edge. This is due to the emissivity of these lines which peaks at the IF where the temperature reaches a maximum (see Fig. 2). The difference between the centre and the edge is about a factor of 10 in $\lambda$ 6584 and $\sim$ 50 for $\lambda$ 3727. The line profiles (shown in Fig. 4) at different impact parameters all show the thermal width corresponding to gas at rest.

Fig. 5 depicts the expansion phase. $\lambda$ 3727 and $\lambda$ 6584 now increase smoothly towards the edge and $\lambda$ 5007 presents a very rounded form. These features are produced by the lower density and the flatter temperature distribution obtained as the H II region expands. This is quite clear in the surface brightness distribution of H$\beta$ with a gradient change over 9–10 pc corresponding to the head of the RW position. Another important feature is that $\lambda$ 6300 emerges at the edge of the region. This is caused by the development of a high-density shocked layer ahead the IF. Between the IF and this layer there is a zone where oxygen is mostly neutral but the electronic density is high enough to excite the $\lambda$ 6300 line. Mallik (1975) found that lines of neutral species ($O^0$ and $N^0$) can be emitted only in the transition region since they require the presence of both neutrals and electrons for their formation. Note that in equilibrium models of H II region (Rubin 1968) the [O I] and [N I] lines are extremely weak. Regarding the line profiles, $\lambda$ 5200, $\lambda$ 6584 and $\lambda$ 6300 show

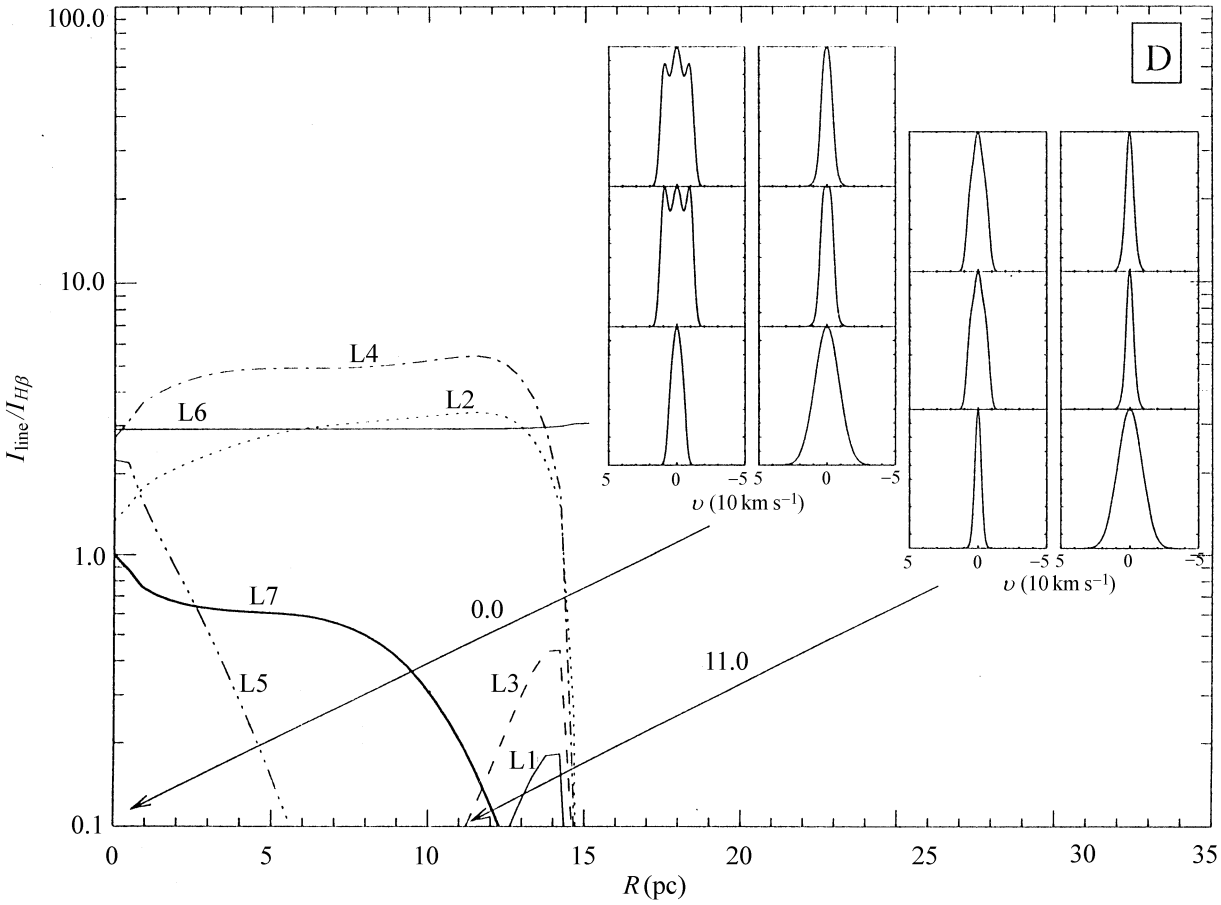


**Fig. 6.** Surface brightness relative to H$\beta$ and line profiles for the model D (see Fig. 3). The symbols and arrows have the same meaning as in the Fig. 4.

splitting with profiles centred at $V \approx 2-3$ km s$^{-1}$. The $\lambda$ 6584 line is thus an important kinematical probe due to its high luminosity and its ability to split even at low gas velocities ($<$ 10 km s$^{-1}$).

Fig. 6 shows results during the recombination phase. The intensities of $\lambda$ 3727 and $\lambda$ 6584 now present a flatter distribution and the lines of the neutral species $\lambda$ 6300 and $\lambda$ 5200 are enhanced at the leading edge of the IF. The profiles of $\lambda$ 6300 and $\lambda$ 5200 present two components across the centre of the nebula, one at the centre with $V = 0$ km s$^{-1}$ and the other at $V = 10$ km s$^{-1}$, while other lines show only one maximum. This two components corresponds to a velocity profile that grows nearly linear from the centre to the edge of the nebula where it reaches a velocity of $V = 10$ km s$^{-1}$. The lines of the higher ions do not present this double component because with the recession of their Strömgren spheres they are confined to the centre of the nebula.

Finally, Fig. 7 displays the phase of reionization. The $\lambda$ 6300 and $\lambda$ 5200 lines now form an extended ring bordering the H II region. The intensity of H$\beta$ is however very low in this part of the region and the possibility of observing this enhancement of the neutral lines at the edge of old H II regions would be scarce.

Summarizing evolving H II region in a low constant medium lead through their expansion to an enhancement at the outer edge of lines of neutral species $\lambda$ 6300 and $\lambda$ 5200. As the evolution proceeds and more gas is accumulated into the shocked layer, the intensity of these lines increases. Moreover, they can show double and multiple components during this phase. When the star leaves the main sequence the narrow outer rings of $\lambda$ 6300 and $\lambda$ 5200 become broader but their surface brightness decreases. The detection of these broadened rings in $\lambda$ 6300 and $\lambda$ 5200 would be a clear trace of very evolved H II regions. However, the $\lambda$ 6584 line emitted in the fully ionized zone is a good indicator of expansion; it splits even at low expansion speeds $\Delta V < 10$ km s$^{-1}$.

### *4.3. Diagnostic diagrams*

Baldwin, Phillips & Terlevich 1981 (hereafter BPT) explored the parameter space of several emission-line quotients to find that different excitation type objects (H II regions, PNe, shocked ionized sources, etc.) occupy well defined zones in what they called diagnostic diagrams. Fig. 8 shows three of these frequently used diagnostic diagrams where the corresponding line

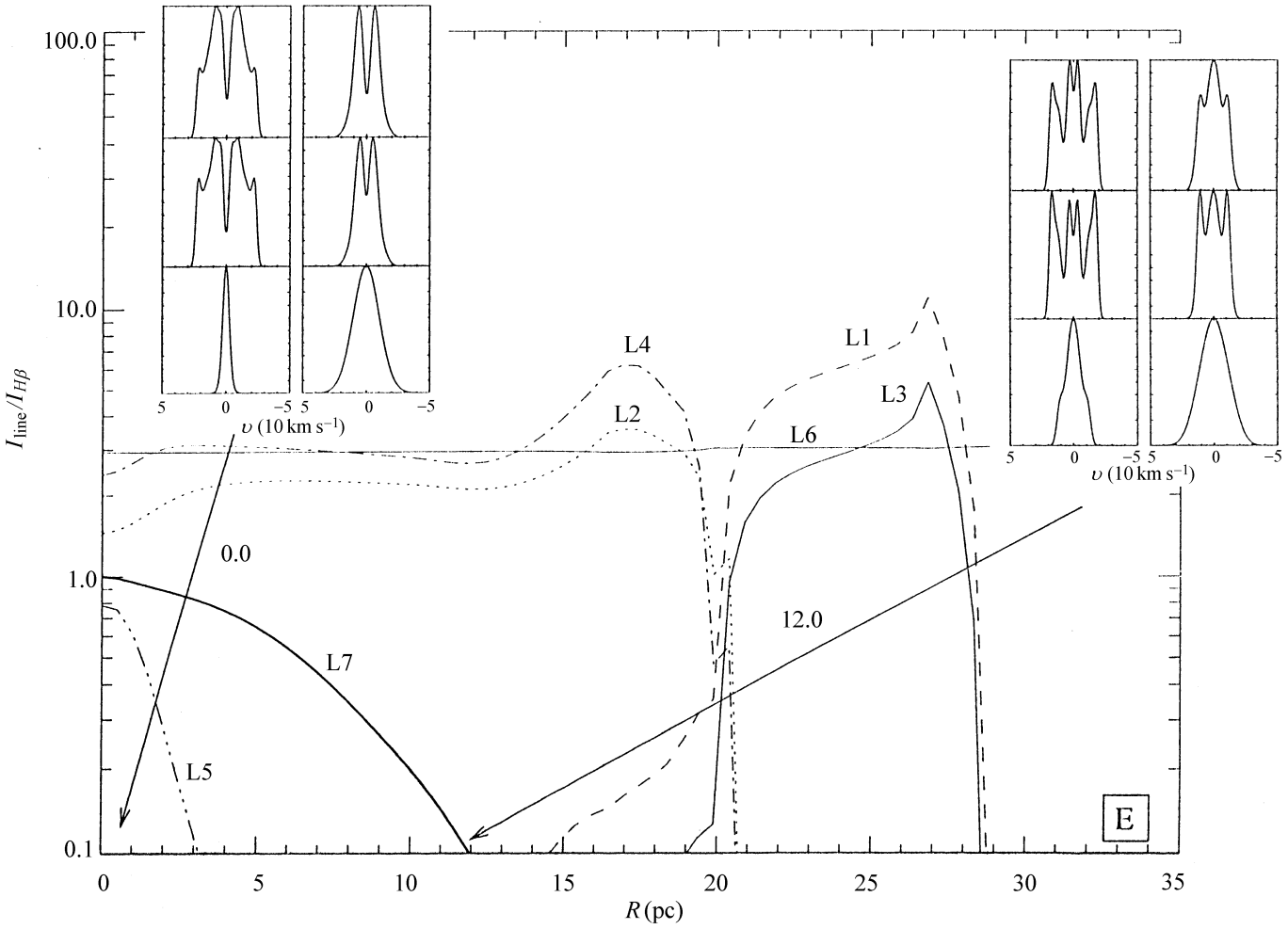


**Fig. 7.** Surface brightness relative to H$\beta$ and line profiles for the model E (see Fig. 3). The symbols and arrows have the same meaning as in the Fig. 4.

ratios of the models calculated in the preceding sections have been plotted. In these diagrams both evolution and spatial sequences are shown. The line quotients integrated over the whole spherical nebula are displayed with large black squares labelled with the corresponding capital letter of the model presented in Sect. 4.1. The sequence given by these line ratios begins in the high-excitation part of the diagrams and evolves towards the low-excitation part. Fig. 8 also displays the envelope of the area filled by the set of 80 Galactic and extragalactic H II regions compiled by BPT (area delimited by a dashed line) and their fit made with an excitation model to these regions (dash-dotted line). The sequence of large squares follows the general trend of the fit but falls slightly outside the area defined by the observations. Fig. 8 also shows the spatial sequences of the line quotients integrated at different impact parameters for each model. The beginning of the spatial sequence is traced by a small black square, labelled with small letters representing every model, and correspond to the line ratios obtained across the centre of the region, i.e. with an impact parameter equal to 0. The rest of the impact parameters are traced with circles of smaller size as we move towards the edge of the nebula and each spatial sequence is joined by a dotted line. Note that all spatial sequences resembles the form of the fit by BPT with the lowest excitation obtained at the edge of the nebula, except for model A(a). This departure is caused by the temperature peak at the IF in the initial model. The collisionally excited lines are strongly temperature dependent while the recombination lines of hydrogen dependent weakly on $T$. An increment in temperature tends therefore to increase the quotient between the collisionally excited lines and the recombination lines of hydrogen. Finally, note that the evolution or sequence followed by the small squares falls well into the observational area of H II regions.

The diagnostic diagrams are a powerful method of determining the physical conditions of ionized nebula and probably also their evolutionary stage. Here we have drawn the sequence for a fixed set of initial conditions (density, ionizing flux and abundances). The use of other initial conditions and their impact on the diagnostic diagrams will be the subject of a forthcoming communication.

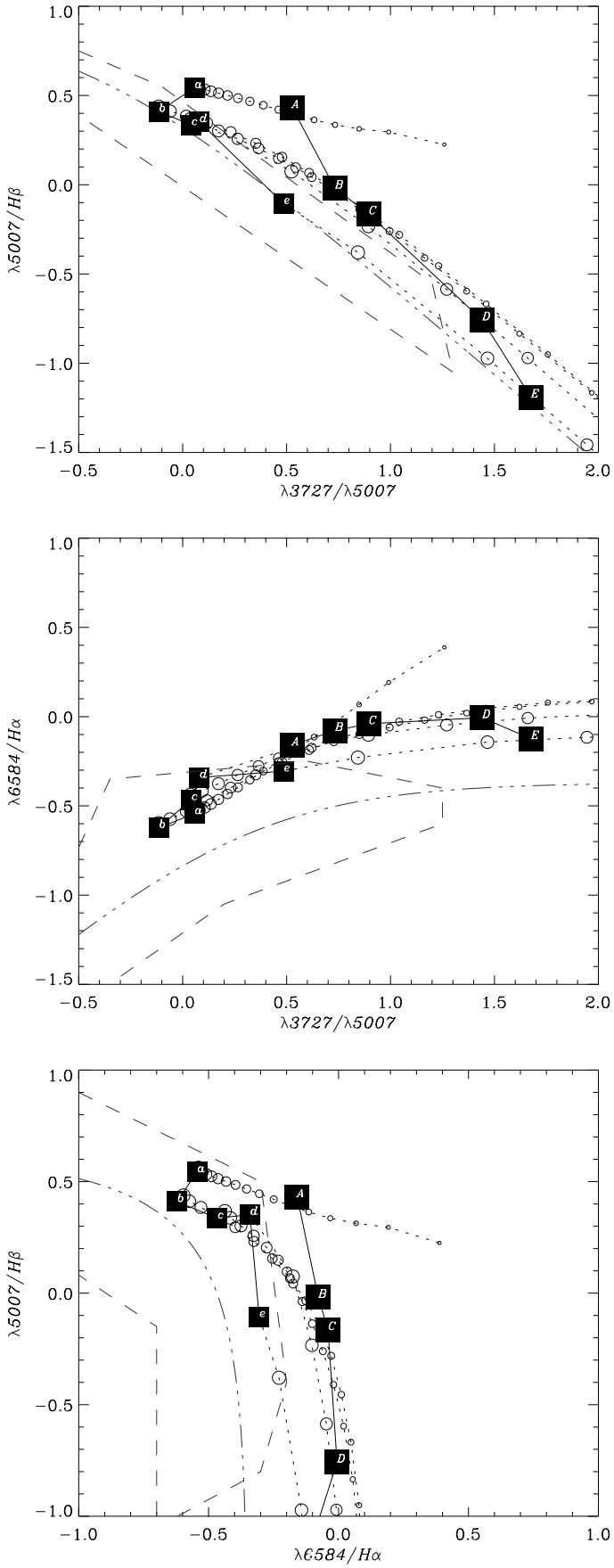


**Fig. 8.** Diagnostic diagrams. Large black squares indicate the line quotient corresponding to the whole spherical nebula for each model (labelled A, B, C, D, E and F). The small black squares indicate the line quotient corresponding to the line of sight across the center of the nebula, i.e. impact parameter equal to 0, for each model (labelled a, b, c, d, e and f). The line quotient corresponding to other impact parameters are plotted with circles of smaller size for larger impact parameters. The large and small black squares have been joined by a continuous line in order to indicate evolution, and the circles have been joined by a dotted line in order to indicate the spatial sequence in each model. The dashed-dotted line is a fit to a set of 80 Galactic and extragalactic H II regions (BPT) and the area delimited by a dashed line is the approximated envelope to $\sim$ 80 % of these H II regions.

## 5. Conclusions

We have presented the results obtained with a new hydrocode which also calculates at every time step the ionization structure of a nebula. The ionization of the hydrogen and helium is calculated time-dependently and the ionization structure of carbon, nitrogen, oxygen and neon is performed under a steady-state approximation with up to five stages of ionization. The code includes the diffuse radiation from the recombinations of hydrogen and helium in two different approximations, the OTS approximation and the outward approximation. The checks performed with a widely used steady-state photoionization code demonstrate that, despite the approximations made, the calculation of the ionization structure and the resultant temperature distribution are quite precise. We have reviewed the evolution of H II regions in a low constant density medium (the standard case) and we will use it as the reference frame for future calculations. The expansion of H II regions is characterized by a faint and narrow ring in the emission of $\lambda$ 6300 and $\lambda$ 5200 which becomes broader and of lower intensity when the region enters its recombination and reionization phases. The analysis of the line profiles has revealed $\lambda$ 6584 as a good kinematical indicator even at low expansion velocities. The diagnostic diagrams of the models corresponding to both evolution and spatial sequences agree well with the empirical results of BPT.

Future work will include several improvements to the code incorporating the action of winds and supernova explosions and more physical processes. The evolution of a giant H II region powered by a massive star cluster will be the topic of our next communication.

*Acknowledgements.* JR-G would like to express his thanks to the *Deutsche Forschungsgemeinschaft* (DFG) for its financial support during part of this work. GT-T gratefully acknowledges the Banco Bilbao Vizcaya foundation for a visiting professorship at the University of Cambridge. We also would like to thank Dr. T. Mahoney for a careful reading of the manuscript.

## Appendix A: treatment of the diffuse field

The ionized gas also contributes to the radiation field through the capture of free electrons, hydrogen and helium ions. For a nebula which is optically thick in the Lyman continuum a good approximation is to suppose that the photons are absorbed in a local environment near the place where the recombination has occurred, i.e. the OTS approximation. This allows the use of the local variables, $x$, $y$, $z$, $T$ and $\rho$ in order to calculate the diffuse radiation and so it is not necessary to solve the transport equation. Recombinations to the ground levels of the $H^0$ produce an emission centred at frequencies $\nu \sim \nu_0$ and, as a consequence, it is entirely absorbed by hydrogen. In the OTS approximation this emission can be easily accounted for by considering only recombinations to the excited levels of hydrogen ($n \geq 2$) in both the ionization and the energy equations. The inclusion of the diffuse photons that ionize helium is not as direct as with hydrogen. The recombinations to the ground levels of $He^0$ and $He^+$ can ionize both the hydrogen and the helium because these photons are emitted with energies greater than $h\nu_1$ = 24.6 eV and $h\nu_2$ = 54.4 eV, respectively. The photoionization terms for these diffuse photons can be written as

$$n_i \Upsilon_i^{j,\mathrm{Lc}} = n_j \zeta_i^j n_e \alpha_{1,j}(T)$$
$$\text{with} \qquad \zeta_i^j = \frac{n_i\, a_{\nu_j,i}}{\sum_k n_k\, a_{\nu_j,k}} \tag{A1}$$

where $i$ = $H^0$, $He^0$ and $He^+$ and $j$ = $He^0$ and $He^+$.

The recombinations to the excited levels of $He^0$ and $He^+$ (recombinations to the $n \geq 2$ level) can also produce photons able to ionize the $H^0$ and $He^0$. The photoionization terms can be written as in Eq. (A1) substituting $\alpha_{1,j}(T)$ by $\eta_j \alpha_{B,j}(T)$, where $\eta_j$ is the efficiency of photoionization, i.e. the probability that each transition $n = 2 \rightarrow n = 1$ could produce an ionizing photon, where now $i$ = $H^0$ and $He^0$ and $j$ = $He^0$ and $He^+$.

The OTS approximation is not as precise in the thermal balance as it is in the ionization balance because it does not take into account the fact that photons emitted after recombination may have different energies so that different penetration depths into the nebula, and thus some of these cannot be absorbed locally. For this reason we have solved for the transport of the diffuse field using the outward approximation (Williams 1967), i.e. each cell may receive ionizing photons from all inner cells. To calculate the radiation intensity $I_\nu^{\mathrm{d}}(R,\theta)$ at each point of the nebula we have built a grid of rays with impact parameters ($b_l$) at different radius. Then, given that $I_\nu^{\mathrm{d}}(R_k, b_l)$ is equivalent to know $I_\nu^{\mathrm{d}}(R_k, \theta_l)$ as in spherical symmetry, $\sin\theta_l = \sqrt{1-(b_l/R_k)^2}$. The radiative transport along each ray with impact parameter $b_l$ is then solved:

$$I^{\mathrm{d}}(R_k, b_l) = \sum_{j=j(l)}^{k} S_j (e^{-t_{k,j}(b_l)} + e^{-t'_{k,j}(b_l)})(1 - e^{-T_j(b_l)}), \tag{A2}$$

for $k = 1, \ldots, K$, and $l = l(k), \ldots, L$, and with

$$T_j(b_l) = \tau_j(b_l) - \tau_{j-1}(b_l),$$
$$t_{k,j}(b_l) = \sum_{i=j+1}^{k} T_i(b_l),$$
$$t'_{k,j}(b_l) = \sum_{i=j-1}^{j(l)} T_i(b_l) + \sum_{i=j(l)}^{k} T_i(b_l),$$
$$\tau_j(b_l) = \sum_{i=j(l)}^{j} \kappa(R_i)(z_{i,l} - z_{i-1,l}), \tag{A3}$$

where $z_{i,l}$ is the coordinate along the ray ($z_{i,l}^2 = R_i^2 - b_l^2$) and $S = \jmath/\kappa$ is the gas source function (we have omitted the dependence on $\nu$ for clarity) and $\jmath$ and $\kappa$ are correspondly the emissivity and the gas opacity. The mean intensity is then calculated through a weighted summing over the rays:

$$J^{\mathrm{d}}(R_k) = \sum_{l=l(k)}^{L} I^{\mathrm{d}}(R_k, b_l)\omega(\mu_{k,l}),$$
$$\text{with} \qquad \sum_{l=l(k)}^{L} \omega(\mu_{k,l}) = 1. \tag{A4}$$

## Appendix B: line transfer

As output, the hydrodynamical models produce a set of magnitudes: density, temperature, velocity, etc, at each spatial location, but these can only be related to observable quantities if they are used to calculate either surface brightness or line profiles.

To solve the radiative transport along a line of sight we used the method described by Yorke (1982). The line intensity is given by

$$I_{\nu,i} = I_{\nu,i-1}e^{-\Delta\tau_{\nu,i}} + \int_{\tau_{\nu,i-1}}^{\tau_{\nu,i}} S_\nu(t)e^{-(\tau_{\nu,i}-t)}dt, \tag{B1}$$

where $\Delta\tau_{\nu,i} = \tau_{\nu,i} - \tau_{\nu,i-1}$, assuming that the continuum contribution to the line is negligible. If the source function $S_\nu$ varies linearly with optical depth, Eq. (B1) can be integrated to yield

$$\begin{aligned} I_{\nu,i} \;=\; & I_{\nu,i-1}e^{-\Delta\tau_{\nu,i}} + S_{\nu,i-1}\left[\frac{1-e^{-\Delta\tau_{\nu,i}}}{\Delta\tau_{\nu,i}} - e^{-\Delta\tau_{\nu,i}}\right] \\ & + S_{\nu,i}\left[1 - \frac{1-e^{-\Delta\tau_{\nu,i}}}{\Delta\tau_{\nu,i}}\right]. \end{aligned} \tag{B2}$$

The emissivity and the opacity are $\jmath(\nu') = \jmath_0\phi_e(\nu')$ and $\kappa(\nu') = \kappa_0\phi_a(\nu')$ where $\jmath_0$ and $\kappa_0$ are the values at the line centre. $\nu'$ is the frequency in the ion reference system, which is displaced from the frequency at rest $\nu$ by the Doppler effect, i.e. $\nu' = \nu/(1+u\cdot\mu/c) \approx \nu(1-u\cdot\mu/c)$, assuming $u \ll c$, where $u\cdot\mu$ is the velocity component along the line of sight. After complete redistribution $\phi_e(\nu') = \phi_a(\nu')$ one obtains

$$\phi(\nu') = \frac{1}{\sqrt{\pi}\Delta\nu_T}\exp\left\{-\left[\frac{\nu'-\nu_0}{\Delta\nu_T}\right]^2\right\}, \tag{B3}$$

where $\Delta\nu_T = \sqrt{2kT/m}\;\nu_0/c$ is the line thermal width. As the emissivity and the opacity have the same frequency dependence the source function $S_\nu$ is independent from the frequency, and in the Eq. (B2) only the optical depth remains as a function of the frequency:

$$\begin{aligned} \Delta\tau_{\nu,i} \;=\; & \int_{s_{i-1}}^{s_i}\kappa_\nu\,ds = (\kappa_0)_{\nu,i}\int_{s_{i-1}}^{s_i}\phi(\nu')\,ds = \\ =\; & \frac{(\kappa_0)_{\nu,i}\Delta s_i c}{2\nu_0\Delta(u\mu)_i}\left\{\mathrm{erf}\,(y+\Delta y) - \mathrm{erf}(y)\right\}, \end{aligned} \tag{B4}$$

where

$$y \equiv \frac{\nu-\nu_0}{\Delta\nu_T} + \frac{\nu}{\Delta\nu_T}\frac{(u\mu)_{i-1}}{c},\; \Delta y \equiv \frac{\nu}{\Delta\nu_T}\frac{\Delta(u\mu)_i}{c}, \tag{B5}$$

$\mathrm{erf}(z) = \sqrt{\pi}/2\int_0^z e^{z^2}\,dz$ is the error function and we have supposed that the velocity component $u\cdot\mu$ varies linearly in the interval $\Delta s_i$, i.e. $\Delta(u\mu)_i = ((u\mu)_i - (u\mu)_{i-1})/\Delta s_i$. $s_i$ is the coordinate along the line of sight. Finally the surface brightness can be determined from the integration over all frequencies of $I_\nu$.

## References


Aldrovandi, S. M. V., Péquinot, D. 1973, A&A 25, 137
Baldwin, J. A., Phillips, M., Terlevich, R. 1981, PASP 93, 5, (BPT)
Beltrametti, M., Tenorio-Tagle, G., Yorke, H. W. 1982, A&A 112, 1 (BTY)
Bodenheimer, P., Tenorio-Tagle, G. Yorke, H. W. 1979, ApJ 233, 8
Butler, S. E., Heil, T. G., Dalgarno, A. 1980, ApJ 241, 442
Butler, S. E., Dalgarno, A. 1980, ApJ 241, 838
Cantó, J., Daltabuit, E. 1974, Rev. Mex. Astron. Astrofís. 1, 5
Dalgarno, A., McCray, R. A. 1972, ARA&A 10, 375
Ferland, G. J. 1990, *HAZY: A Brief Introduction to CLOUDY*, V.76.03, 1990
Franco, J. 1981, Rev. Mex. Astron. Astrofís. 27, 475
Franco, J., Tenorio-Tagle, G., Bodenheimer, P. 1990, ApJ 349, 126
Harrington, J. P., Seaton, M. J., Adams, S., Lutz, J. H. 1982, MNRAS 199, 517
Manfroid, J. 1976, Ap&SS 41, 39
Mallik, D. C. V. 1975, ApJ 197, 355
Mathews, W. G. 1965, ApJ 142, 1120
Mendoza, C. 1983, in Planetary Nebulae, IAU Symp. 103, D. R. Flower, ed. (Dordrecht: Reidel), p. 143
Osterbrock, D. E. 1989, Astrophysics of Gaseous Nebulae and Active Galactic Nuclei (Mill Valley: University Science Books)
Reilman, R. F., Manson, S. T. 1979, ApjS 40, 815
Richtmyer, R. D., Morton, K. W. 1967, Difference Methods for Initial-Value Problems, 2nd. edn. (New York: Interscience Publishers)
Rodríguez-Gaspar, J. A., Tenorio-Tagle, G., Franco, J. 1995, ApJ 451, 210
Rubin, R. H. 1968, ApJ 153, 761
Seaton, M. J. 1958, Rev. Mod. Phys. , 80, 979
Seaton, M. J. 1959, MNRAS 119, 81
Spitzer, L. 1978, Physical Processes in the Interstellar Medium (New York: Wiley)
Strömgren, B. 1939, ApJ 89, 526
Tenorio-Tagle, G. 1976, A&A 53, 411
Tenorio-Tagle, G. 1979, A&A 71, 59
Tenorio-Tagle, G., Beltrametti, M., Bodenheimer, P., Yorke, H. W. 1982, A&A 112, 104 (TBBY)
Tenorio-Tagle, G., Bodenheimer, P., Noriega-Crespo, A. 1986, in Workshop on Model Nebulae, D. Pequinot, ed. (Paris: Observatoire de Paris), p. 178
Williams, R. E. 1967, ApJ 147, 556
Yorke, H. W. 1982, in Astrophysical Radiation Hydrodynamics, K. A. Winkler, M. L. Norman (Dordrecht: Reidel), p. 141
Yorke, H. W., Tenorio-Tagle, G., Bodenheimer, P. 1983, A&A 127, 313
Yorke, H. W., Tenorio-Tagle, G. Bodenheimer, P. 1984, A&A 138, 325
Yorke, H. W. 1986, ARA&A 24, 49


This article was processed by the author using Springer-Verlag LaTeX A&A style file *L-AA* version 3.